Enhanced carrier transport and bandgap reduction in sulfur-modified $BiVO_4$ photoanodes

Marlene Lamers[†], Wenjie Li[§], Marco Favaro[†], David E. Starr[†], Dennis Friedrich[†], Sheikha Lardhi[¶], Luigi Cavallo[¶], Moussab Harb[¶], Roel van de Krol[†], Lydia H. Wong[§], Fatwa F. Abdi[*†]

[†] Institute for Solar Fuels, Helmholtz-Zentrum Berlin für Materialien und Energie GmbH, Hahn-Meitner-Platz 1, Berlin 14109, Germany

[§] School of Materials Science and Engineering, Nanyang Technological University, Nanyang Avenue, Singapore 639798

[¶] KAUST Catalysis Center (KCC), Physical Sciences and Engineering Division (PSE), King Abdullah University of Science and Technology (KAUST), Thuwal 23955-6900, Saudi Arabia

E-mail: fatwa.abdi@helmholtz-berlin.de

ABSTRACT: Recent progress on bismuth vanadate ($BiVO_4$) has shown it to be among the highest performing metal oxide photoanode materials. However, further improvement, especially in the form of thin film photoelectrodes, is hampered by its poor charge carrier transport and its relatively wide bandgap. Here, sulfur incorporation is used to address these limitations. A maximum bandgap decrease of ~0.3 eV is obtained, which increases the theoretical maximum solar-to-hydrogen efficiency from 9 to 12%. Hard X-ray photoelectron spectroscopy (HAXPES) measurements as well as density functional theory (DFT) calculations show that the main reason for the bandgap decrease is an upward shift of the valence band maximum. Time-resolved microwave conductivity measurements reveal an ~3 times higher charge carrier mobility compared to unmodified $BiVO_4$, resulting in a ~70% increase in the carrier diffusion length. This work demonstrates that sulfur doping can be a promising and practical method to improve the performance of wide-bandgap metal oxide photoelectrodes.

1. Introduction

Photoelectrochemical (PEC) water splitting is a renewable pathway to store energy from sunlight in the form of hydrogen and oxygen. The process utilizes a semiconductor photoelectrode immersed in an electrolyte to absorb sunlight, separate electrons and holes, and promote the water oxidation or reduction reaction at its surface.[1] While one can also achieve this by combining a commercial photovoltaic cell and an electrolyzer (PV-E), the PEC route offers additional advantages.[2] First, the operating current density of PEC systems is 10-100× lower than that of PV-E, which relaxes the demands on the hydrogen and oxygen evolution catalysts. Additionally, due to the integration of light absorption and electrochemistry, PEC systems are able to take advantage of the solar heat in order to enhance the electrochemical reaction kinetics and thereby improve the overall efficiency.[2]

Metal oxides are attractive as photoelectrodes due to their relative stability in aqueous solutions, low cost, and non-toxicity.[3-5] Among the various metal oxides, bismuth vanadate ($BiVO_4$) is particularly interesting; it appears to be fairly defect-tolerant and is currently the highest performing metal oxide photoanode material.[6-8] The highest reported photocurrent of $BiVO_4$ is already within 90% of the maximum theoretical photocurrent of 7.5 mA cm^{-2} (based on the assumption that all AM1.5 photons with energy higher than the bandgap of 2.4 eV are collected as photocurrent).[9] This record photocurrent was achieved by Pihosh et al. through nanostructuring; a thin layer

of $BiVO_4$ was deposited on WO_3 nanorods to form a guest-host nanostructured photoelectrode and orthogonalize the optical absorption and charge transport direction.[10, 11]

Despite these encouraging results, two limitations remain for $BiVO_4$. First, high photocurrents (> 5 mA cm^{-2}) have only been achieved with nanostructuring, since the carrier transport properties of $BiVO_4$ are relatively poor (reported carrier mobilities are in the range of 10^{-2} - 10^{-1} $cm^2 V^{-1} s^{-1}$).[12] Nanostructuring, however, introduces extensive optical scattering, which adds additional complexities to the design of the resulting solar water splitting device.[9, 13] Second, the fact that 90% of the maximum theoretical photocurrent has already been achieved suggests that the current performance is limited by its relatively wide bandgap.[6, 14] To further increase the photocurrent, the range of optical absorption of $BiVO_4$ needs to be extended by reducing its bandgap. Solving these two limitations will allow further improvement of $BiVO_4$ photoanodes.

One approach to address this limitation is by cation doping like e.g. substituting V with Sb or Bi with Mn or Fe.[15-18] Anion substitution is another possible way to simultaneously address both poor charge carrier mobilities and bandgap reduction in $BiVO_4$. The valence band maxima of most metal oxides, including $BiVO_4$, are mainly composed of O 2p orbitals. Anion substitution with elements having higher orbital energies (e.g., sulfur) could potentially shift the valence band maximum upwards and decrease the bandgap. This modification may also enhance the carrier transport properties. For example, DFT calculations showed that sulfur incorporation in α-Fe_2O_3 reduces the bandgap and increases the carrier mobility due to a decrease in the carrier effective mass.[19] Sulfur-doped ZnO and WO_3 also have superior photoelectrochemical (PEC) performance as compared to the pristine material, due to an increase in their light harvesting ability.[20, 21] Despite this promise, reports on sulfur incorporation in $BiVO_4$ are limited.[22, 23] Previous work on powder-based photocatalysts showed that incorporating sulfur into the $BiVO_4$ lattice leads to a slight decrease of its optical bandgap and an enhancement of its activity towards methylene blue degradation. However, the range of sulfur concentration in these studies was very limited, and the nature of sulfur incorporation as well as the improvement mechanism were not clear. To unravel the interplay between the concentration of sulfur and the structural, optical, and electronic properties of $BiVO_4$ photoelectrodes, systematic studies on thin film $BiVO_4$ samples are needed.

In this work, we successfully incorporated sulfur in $BiVO_4$ thin films using a post-annealing treatment in a sulfur-rich atmosphere. By adjusting the sulfur partial pressure its concentration in $BiVO_4$ could be controlled, resulting in a bandgap decrease of up to ~0.3 eV. Hard X-ray photoelectron spectroscopy (HAXPES) and DFT calculations show experimentally and theoretically that this bandgap reduction is caused by an upward shift of the valence band maximum, therefore maintaining the favorable band alignment of $BiVO_4$ with respect to the water oxidation and reduction potentials. At the same time, the carrier mobility of the sulfur-incorporated $BiVO_4$ is increased by a factor of ~3. This study demonstrates the effectiveness of sulfur incorporation to address the limitations of $BiVO_4$ photoanodes.

2. Results and discussion

2.1 Optical and structural characterization

Spray-deposited $BiVO_4$ films were subjected to annealing at different sulfur (S) partial pressures (see Experimental Section). **Figure 1a** shows a photograph of the films annealed at 350 °C for 2 hours at S partial pressures between 0 and 3×10^{-3} bar. The color of the films clearly changes from yellow to dark brown with increasing sulfur pressure. A similar color change was also obtained when maintaining the same sulfur partial pressure but increasing the annealing temperature (see Figure S1). Tauc analysis was performed on films annealed at 350 °C in order to determine the bandgap. The bandgap of $BiVO_4$ is known to be indirect,[14] but the relatively large amount of scattering prevented an indirect bandgap Tauc analysis. Since the direct bandgap is only 0.2 eV larger than the indirect one due to the modest dispersion of the $BiVO_4$ bands, we used a direct bandgap Tauc analysis (Figure S2). As shown in **Figure 1b**, the direct bandgap decreases with increasing sulfur partial pressure from 2.56 eV for the unmodified film to 2.32 eV for the film annealed in sulfur partial pressure of 3×10^{-3} bar.

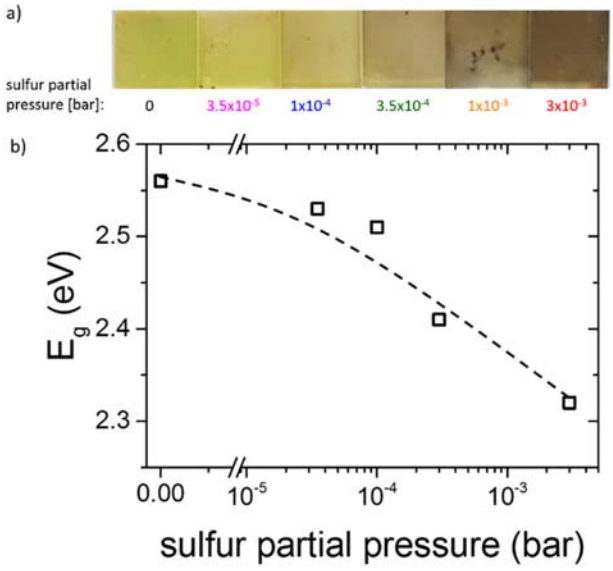

Figure 1. (a) Photograph of the sulfur incorporated $BiVO_4$ films on quartz substrates annealed at 350 °C for 2 hours at different sulfur partial pressures. **(b)** The direct bandgap (E_g) of $BiVO_4$ film decreases with increasing sulfur partial pressure.

To confirm that the optical absorption change is indeed caused by the presence of sulfur inside the $BiVO_4$, bulk-sensitive X-ray fluorescence (XRF) and surface-sensitive X-ray photoelectron spectroscopy (XPS) measurements were performed. XRF reveals that the sulfur-to-vanadium (S/V) ratio increases from 0 in the control film to ~1 in the film annealed in 3×10^{-3} bar of sulfur partial pressure (**Figure 2**). These values are compared with the S/V ratios obtained from XPS (more detailed XPS analysis can be found later in the manuscript). The S 2s peak was chosen to quantify the amount of sulfur, since the more common S 2p peaks overlap with the more intense Bi 4f

peaks. Figure 2 shows that the XPS values are in very good agreement with the XRF results, suggesting that the sulfur is homogeneously incorporated in the $BiVO_4$ films (i.e., no bulk or surface segregation).

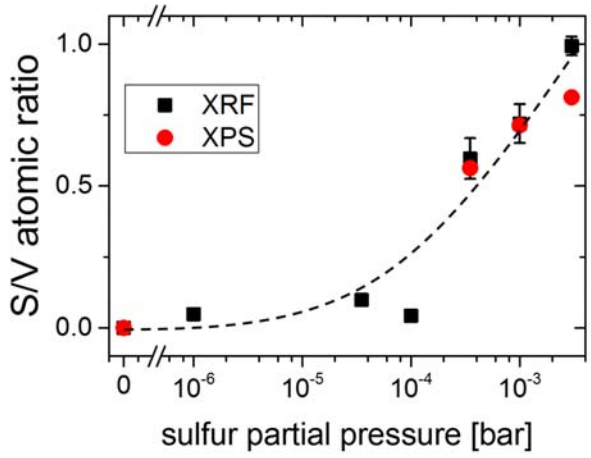

Figure 2. S/V atomic ratio in $BiVO_4$ films as a function of the sulfur partial pressure during post-annealing, as obtained by X-ray fluorescence (XRF) and X-ray photoelectron spectroscopy (XPS).

Figure 3a shows the X-ray diffractograms of the $BiVO_4$ films annealed at 350 °C and varying sulfur partial pressures. All films show the monoclinic $BiVO_4$ phase (clinobisvanite; space group: I2/b JCPDS card No. 14-0688), which is the most photoactive phase,[24] but at sulfur partial pressure of 10^{-3} bar and above Bi_2S_3 starts to be formed. This is further confirmed by Raman spectroscopy (Figure S3), which shows additional peaks at wavenumbers of 183, 239 and 260 cm^{-1}, all of which can be assigned to Bi_2S_3.[25, 26] The temperature and pressure region in which Bi_2S_3 is formed is mapped in the pressure-temperature phase diagram shown in **Figure 3b**. The color of each point corresponds to the relative amount of Bi_2S_3 and the gray line indicates the boundary (limited to the resolution of our data points) at which phase segregation starts to occur.

Since phase segregation is undesirable in our study, further analysis is limited to $BiVO_4$ thin films that do not contain any Bi_2S_3. In particular, we focus our study on $BiVO_4$ films annealed at 350 °C in a sulfur partial pressure of up to 3.5×10^{-4} bar.

The oxidation state of sulfur within the $BiVO_4$ lattice was investigated using lab-based XPS. The S 2s spectra of the $BiVO_4$ film annealed at 350 °C and sulfur partial pressures of 0 and 3.5×10^{-4} bar are shown in **Figure 4a**. A clear peak at 232.4 eV can be observed in the sulfur-incorporated $BiVO_4$, while the control film shows no peak. This peak can be attributed to the sulfur oxidation state of -2 in $BiVO_4$,[27] or sulfates.[28] To distinguish between the two, we utilized hard X-ray photoelectron spectroscopy (HAXPES) to measure the S 1s spectrum (see Figure S4). A peak at ~2478 eV is observed that can be assigned to the oxidation state of -2.[29] This is further confirmed by the fact that no trace of sulfate-containing phase was found in the X-ray diffractogram (Figure 3a) and the Raman spectra (Figure S3).

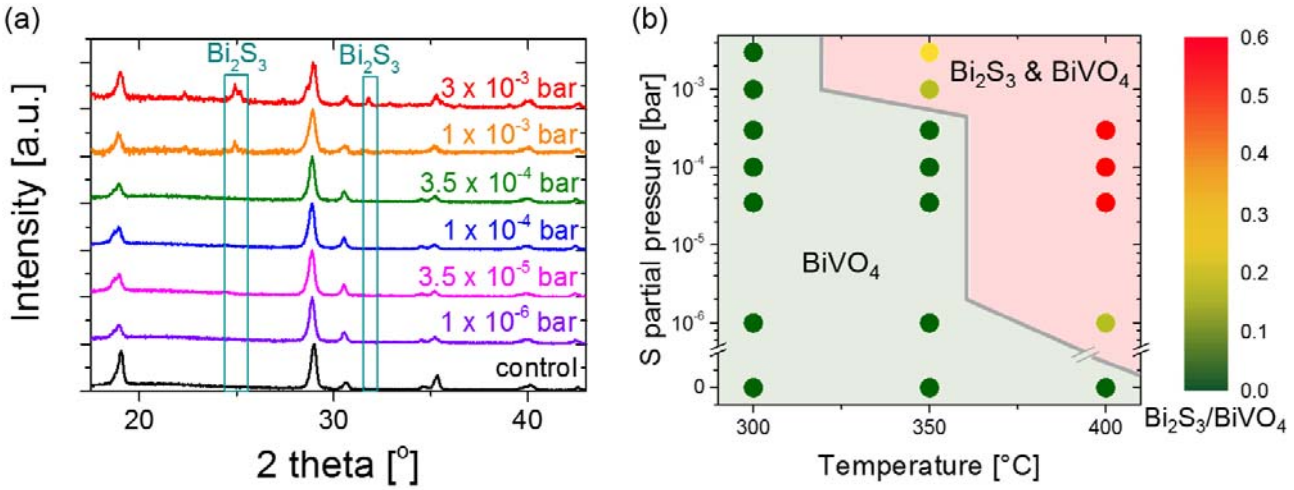

Figure 3. (a) X-ray diffractograms of $BiVO_4$ films annealed at 350 °C in varying sulfur partial pressures. All films show monoclinic phase, but phase segregation into Bi_2S_3 occurs above a sulfur pressure of 3×10^{-4} bar. **(b)** Pressure-temperature phase diagram indicating the phase segregation of sulfur-incorporated $BiVO_4$ and Bi_2S_3 based on the XRD measurements. The color of each points indicates the ratio of the Bi_2S_3 phase to the monoclinic $BiVO_4$ phase. The gray line indicates the boundary (limited to the resolution of our measured data points) at which phase segregation starts to occur.

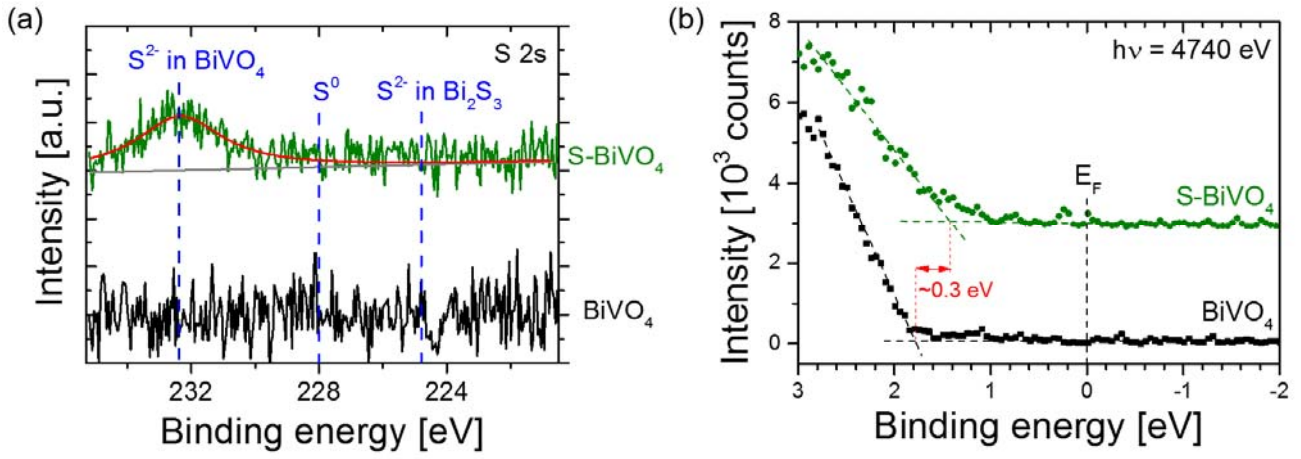

Figure 4. (a) S 2s X-ray photoelectron spectra of the $BiVO_4$ films annealed at 350 °C and sulfur partial pressure of 0 and 3.5×10^{-4} bar. (b) Valence band spectra of the $BiVO_4$ films annealed at 350 °C and sulfur partial pressure of 0 and 3.5×10^{-4} bar measured by hard X-ray photoelectron spectroscopy. The valence band shifts closer to the Fermi level (EF, binding energy = 0 eV) after sulfur incorporation.

Sulfur vapor is composed of S_n molecules, with n ranging from 1 to 8.[30] Based on this, the following substitution reaction presumably occurs in the $BiVO_4$ crystal lattice (in Kröger-Vink notation[31]):

$$S_n(g) + n\, O_O^{\times} \rightleftharpoons n\, S_O^{\times} + (n/2)\, O_2(g) \quad (1)$$

This is supported by the observed shifts of the (121) and (040) X-ray diffraction peaks (Figure S5), which indicate $BiVO_4$ lattice expansion upon substituting O^{2-} (140 pm radius) with S^{2-} (180 pm radius). These shifts were also reported in sulfur-modified $BiVO_4$ powders.[22, 23, 27] This is consistent with a shift of the main Raman peak at ~832 cm^{-1}, which corresponds to the symmetric V-O stretching mode, to lower wavenumbers (see Figure S3).

To investigate the origin of the bandgap change shown in Figure 1, the position of the valence band maximum of the films was determined using HAXPES. **Figure 4b** shows the valence band HAXPES data of the control sample and the sample annealed at a sulfur partial pressure of 3.5×10^{-4} bar. After sulfur incorporation (green curve), the valence band maximum shows a pronounced ~0.3 eV shift to lower binding energy. The magnitude of this shift is in very good agreement with the observed bandgap change (Fig. 1). Assuming that the Fermi level of the S-modified sample has not shifted (i.e., no change in donor density since S and O are isovalent), this suggests that the valence band maximum of $BiVO_4$ shifts upwards upon sulfur incorporation. While the ~0.3 eV shift may seem modest, it increases the theoretical maximum solar-to-hydrogen (STH) efficiency to ~12% (vs. ~9% for pristine $BiVO_4$).

2.2. Density functional theory (DFT) calculation

We performed DFT calculations to understand sulfur incorporation into the $BiVO_4$ monoclinic lattice. 16 ($BiVO_4$) structural model generated from the $2 \times 1 \times 2$ monoclinic supercell was used, which contains a total of 96 atoms (**Figure 5a**). Several configurations for sulfur incorporation were explored: S-linear (Figure S6a), S-random (Figure S6b), S-around Bi (Figure S6c), S-around V (Figure S6d), and well-dispersed S-pairing (Figure 5b). In this calculation, a S/V ratio of 0.63 was chosen (i.e., $BiVO_{3.37}S_{0.63}$), based on the experimental XRF and XPS results (Figure 2). The thermodynamic stability of these structures was investigated using molecular sulfur (S_2) in the gas phase as the source of sulfur (elemental sulfur shows similar behavior); a fixed partial pressure of 3.5×10^{-4} bar and a fixed temperature of 350 °C were chosen, based on the experimental conditions for sulfur incorporation. In an oxygen free atmosphere ($\Delta\mu_O$ = -4 eV), the formation energies (with respect to pristine $BiVO_4$) for the various S-configurations are listed in Table 1. The lowest-energy (i.e., most stable) structure was obtained using the well-dispersed S-pairing configuration, where the 10 S atoms were substituted at O sites that were homogeneously distributed throughout the lattice. In this structure, each pair of S atoms occupies the two nearest neighbor O sites that bridge 2 Bi atoms (see **Figure 5b**). This structure remains the most stable S-containing configuration for the entire range of $\Delta\mu_O$ values, although it starts to become metastable as compared to the pristine $BiVO_4$ at higher $\Delta\mu_O$ (Figure S7). The bond lengths in this S-incorporated $BiVO_4$ are listed in Table S1, along with those for the pristine $BiVO_4$ structure.

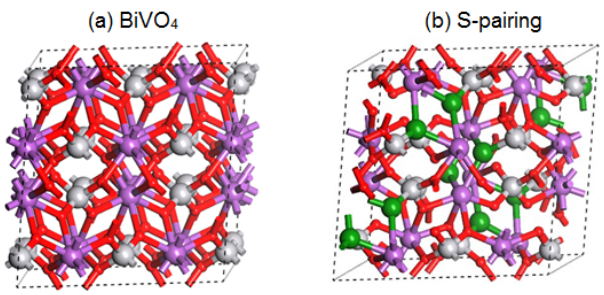

Figure 5. (a) DFT-based crystal structure of pristine $BiVO_4$. **(b)** DFT-based lowest-energy optimized crystal structure of $BiVO_{3.37}S_{0.63}$ material revealing a well-dispersed S-pairing configuration. Bi are in purple, V in gray, O in red, and S in green.

Table 1. Formation energies for the various explored S-configurations in $BiVO_4$ with respect to pristine $BiVO_4$ in an oxygen free atmosphere ($\Delta\mu 0 = -4$ eV) and a temperature of 350 °C, assuming molecular sulfur (S_2) in the gas phase as the source of sulfur and a partial pressure of 3.5×10^{-4} bar.

S-configuration in $BiVO_4$	Formation energy (eV)
no S (i.e., pristine)	0
linear	+0.01
random	-0.14
around Bi	+0.05
around V	+0.07
well-dispersed pairing	-0.25

DFT-based analysis of the electronic structure of $BiVO_{3.37}S_{0.63}$ was carried out by computing the electronic density of states (DOS) as a function of the band energy for the most relevant predicted structure (i.e., well-dispersed S-pairing, Figure 5b). This is compared to that obtained for the unmodified $BiVO_4$ to provide relevant information about any relative shift in the valence or conduction band. We note that DFT calculation using the PBE functional tends to underestimate the bandgap of a material; we therefore are more interested in the trend/shift observed upon S-incorporation and less in the absolute value. The calculated results are shown in **Figure 6**. By comparing the density of states of $BiVO_4$ and $BiVO_{3.37}S_{0.63}$, it can be clearly seen that the valence band is shifted upwards by around 0.4 eV upon S incorporation due to the additional electronic states originated from S 3p orbitals, while the conduction band position remains relatively unchanged. This result is not only in good agreement with the HAXPES measurements (Figure 4b), but also confirms that the origin of the observed bandgap decrease is mainly due to an upward shift of the valence band maximum. Note that the other structural configurations explored (i.e., S-linear, S-random, S-around Bi, and S-around V) revealed much narrower bandgaps as compared to the well-dispersed S-pairing one (see Figure S8)

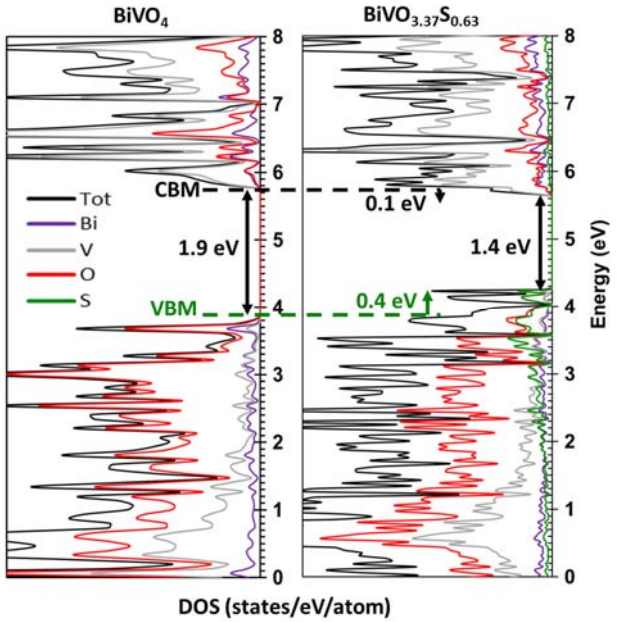

Figure 6. DFT-based computed electronic structure of $BiVO_4$ (left) and $BiVO_{3.37}S_{0.63}$ (right) revealing well-dispersed S-pairing configuration. Contributions from S 3p, O 2p, V 3d, and Bi 6s are shown in green, red, gray, and purple colors, respectively.

2.3. Charge carrier transport and photoactivity of sulfur incorporated $BiVO_4$

With the decrease in bandgap upon sulfur incorporation firmly established, we now turn our attention to the charge carrier transport properties of the films. Time-resolved microwave conductivity (TRMC) measurements were carried out to elucidate how the carrier mobility, the lifetime, and the diffusion length of $BiVO_4$ are affected by the incorporation of sulfur. Pulsed laser illumination with a wavelength of 355 nm was used, which is well above the bandgap for all films. Examples of TRMC curves for unmodified and sulfur-incorporated $BiVO_4$ films are shown in Figure S9. The effective carrier mobility of the films can be obtained from the maximum of these curves ($(\phi\sum\mu_{max})$), and plotted as a function of sulfur partial pressure (i.e., sulfur concentration) in Figure 7. With increasing sulfur concentration, the carrier mobility of $BiVO_4$ systematically increases by up to a factor of 3, from ~0.02 $cm^2V^{-1}s^{-1}$ up to ~0.06 $cm^2V^{-1}s^{-1}$. The effective carrier lifetime can be obtained by fitting the decay of the TRMC curves (Figure S9) with a second order exponential decay function. Sulfur incorporation was found to have only a minor effect on the main lifetime; a carrier lifetime value of ~70 ns was obtained for all samples. Overall, the improved carrier mobility and the constant lifetime results in a ~70% increase of the carrier diffusion length, from ~60 up to ~100 nm.

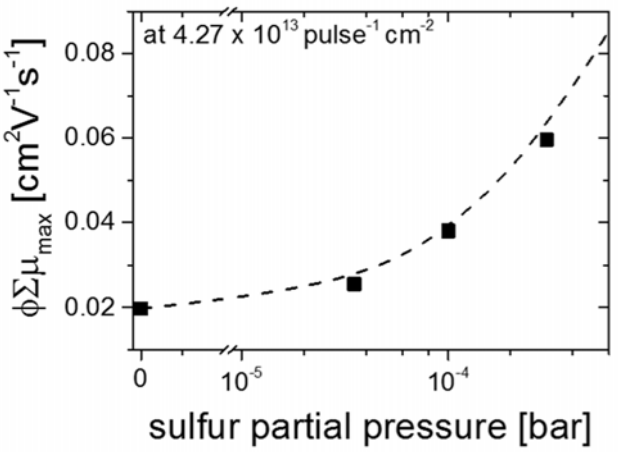

Figure 7. Charge carrier mobility ($\phi\Sigma\mu_{max}$) of $BiVO_4$ films as a function of the sulfur partial pressure during post-annealing (T = 350 °C). A clear improvement of mobility is shown by incorporating S into $BiVO_4$. The mobility values were obtained from time-resolved microwave conductivity signals measured at a laser intensity of 4.27×10^{13} photons $pulse^{-1}cm^{-2}$ and a wavelength of 355 nm.

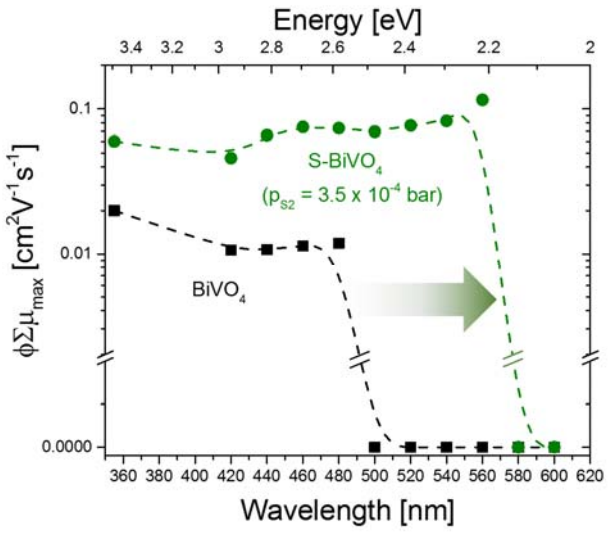

Figure 8. PCAS spectra, i.e., charge carrier mobility ($\phi\Sigma\mu_{max}$) vs. wavelength, of the $BiVO_4$ control sample and the S incorporated $BiVO_4$ sample at sulfur partial pressure of 3.5×10^{-4} bar, as measured by TRMC at a laser intensity of $\sim 4 \times 10^{13}$ photons $pulse^{-1}cm^{-2}$.

To confirm the photoactivity of the S-incorporated sample above the typical bandgap of $BiVO_4$, photoconductivity action spectroscopy (PCAS) measurements were performed. Here, the excitation wavelength of the laser used in TRMC was continuously increased in 20 nm steps from 420 up to 600 nm. For the $BiVO_4$ control sample (black curve in **Figure 8**), no signal was detected above 500 nm (hν = ~2.5 eV), and a carrier mobility of ~0.01-0.02 $cm^2V^{-1}s^{-1}$ was obtained below this wavelength. In contrast, TRMC signals are detected up to 560 nm (hν = ~2.2 eV) for the sulfur-incorporated $BiVO_4$ sample (green curve in Figure 8). The PCAS spectrum also shows a clear increase in carrier mobility to ~0.05-0.1 $cm^2V^{-1}s^{-1}$.

The mobility action spectra (i.e., wavelength-dependent mobility) above imply two important points. First, the shift of the onset wavelength upon sulfur incorporation again confirms the reduction of the bandgap. Second, since TRMC is sensitive only to photo-generated *mobile* carriers, the fact that we observed relatively constant mobility for the sulfur-incorporated $BiVO_4$ up to the band edge suggests that these carriers remain mobile and are not trapped in defect states. In other words, sulfur incorporation not only increases visible light absorption, but also the photoactivity of $BiVO_4$. Similar enhancement has been reported for the sulfur-doped TiO_2, where the absorption as well as the quantum efficiency are extended beyond the bandgap of pristine TiO_2. [32, 33]

The combination of a decrease in the bandgap (i.e., extension of photoactivity) as well as the increased carrier diffusion length suggests that sulfur incorporation in $BiVO_4$ would result in the enhancement of the photoelectrochemical performance. Figure 9 shows that the AM1.5 photocurrent of a pristine $BiVO_4$ film in 0.1 M potassium phosphate (KPi) buffer (pH ~7) with added 0.5 M sodium sulfite (Na_2SO_3) as a hole scavenger (no co-catalyst) is ~1.1 $mAcm^{-2}$ at 1.23 V vs. RHE. This photocurrent is modest compared to our best performing $BiVO_4$,[7, 34] since W- or H-doping and a SnO_2 hole-blocking layer were not used here to exclude any possible convoluted effects due to the interaction between sulfur and these modifications. Upon S-incorporation, the photocurrent increases by ~60% to 1.8 $mAcm^{-2}$ at 1.23 V vs. RHE.

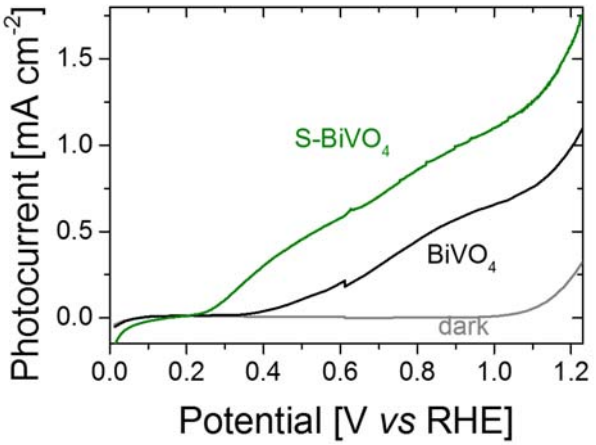

Figure 9. AM1.5 photocurrent-voltage curves of the pristine $BiVO_4$ film and the one annealed in in sulfur partial pressure of 3.5×10^{-4} bar. The electrolyte is 0.1 M potassium phosphate (KPi) buffer (pH ~7) with added 0.5 M sodium sulfite (Na_2SO_3) as a hole scavenger.

We note that part of the increase in photocurrent of the sulfur-modified $BiVO_4$ may be due to photocorrosion. Subsequent cyclic voltammetry measurements of the S-incorporated films show a decrease in photocurrent for the second and third CV

cycles (Figure S10). Since the brownish S-$BiVO_4$ films return to their original yellow color after the photoelectrochemical measurements, we attribute the decrease in photocurrent to re-oxidation (i.e., loss of sulfur) of the films. Similar stability issues are known for many sulfides and oxy-sulfides,[35, 36] and strategies are in place to overcome this limitation.[36-39] Efforts in depositing suitable protection layers and/or co-catalysts, which is beyond the scope of the current study, are currently ongoing and are expected to increase the stability of the S-incorporated $BiVO_4$.

3. Conclusion

We have shown that a simple post-deposition heat treatment in a sulfur vapor atmosphere leads to the homogeneous incorporation of sulfur into thin film $BiVO_4$ photoelectrodes. The sulfur is found to decrease the bandgap and improve the charge carrier transport properties of $BiVO_4$. The maximum bandgap decrease is ~ 0.3 eV. Incorporation of additional sulfur leads to segregation of a Bi_2S_3 phase. Both HAXPES measurements and DFT calculations confirm that this bandgap shift is caused by an upward shift of the valence band maximum. TRMC measurements revealed that the change in absorption onset is also accompanied by an improvement in photoactivity, and the shift in onset wavelength for detecting mobile and photoactive carriers matches well the decrease in the bandgap. The mobility of the charge carriers increases by a factor of ~3 upon sulfur incorporation, resulting in a ~70% longer carrier diffusion length than for unmodified $BiVO_4$. The sulfur-incorporated $BiVO_4$ films show a 60% increase in the AM1.5 photocurrent. Since subsequent I-V curves show a slow but steady decrease in photocurrent, presumably caused by re-oxidation (sulfur loss) of the films, future efforts should be directed towards applying protection layers[40] (e.g., leaky TiO2[37, 41], p-type TCO[42, 43]) and/or co-catalysts on the surface of the film. If this is successful, solar-to-hydrogen efficiencies of up to 12% can be achieved due to the decrease in the bandgap. This shows that sulfur doping is a promising strategy to further improve the photoelectrochemical performance of $BiVO_4$ and possibly other metal oxides that are limited by a large bandgap and poor carrier transport.

4. Experimental Section

Synthesis:

Spray pyrolysis was used to prepare 100 nm-thick $BiVO_4$ films following a previously reported method.[34, 44-46] During the spray pyrolysis, a conducting glass substrate (fluorine-doped tin oxide, TEC7, Pilkington) or quartz substrate (polished, Spectrosil 2000, Heraeus) was placed on a hot plate, and the temperature was set to 450 °C. The precursor solution was 0.4 mmol $VO(C_2H_7O_2)_2$ (99%, Alfa Aesar) and 0.4 mmol $Bi(NO_3)_3.5H_2O$ (98%, Alfa Aesar) in 100 mL solvent consisting of acetic acid (98%, Sigma Aldrich) and ethanol (Sigma Aldrich) in a 1:9 ratio. The solution was sprayed in 100 cycles onto the heated substrate (spray rate ~ 1 nm per cycle), followed by post-annealing in air at 450 °C for 2h. For sulfur incorporation into these films a two-chamber oven was used. In the first part of the oven, excess amount of sulfur powder (Sigma) was heated at temperatures between 90 and 200 °C, creating different sulfur partial pressures between 0 and 3×10^{-3} bar (see Figure S11 for the correlation between the temperature and the respective sulfur partial pressure).[47, 48] Due to the partial pressure difference between the two parts of the oven, the sulfur-rich atmosphere was distributed evenly through both parts to reach an equilibrium. In the second part of the oven, the $BiVO_4$ films were placed and the temperature was varied between 300 and 400 °C. During the sulfur incorporation, the two-chamber oven was further kept under Ar background pressure of 300 mbar.

Materials Characterization:

A Lambda 950 spectrometer (Perkin Elmer) with an integrating sphere (the films were placed inside the sphere) was used to perform UV-Vis spectroscopy in a wavelength range of 320 to 800 nm. Lab-based X-ray photoelectron spectroscopy (XPS) was conducted using a SPECS PHOIBOS 100 analyzer and a X-ray source with a SPECS FOCUS 500 monochromator (Al Kα radiation hν = 1486.74 eV). All spectra were calibrated to the carbon C 1s peak at 284.8 eV, and a Shirley background was subtracted. The atomic ratio was calculated by

$$\text{Atomic ratio (i:j)} = \frac{I_i/S_i}{I_j/S_j} \quad (2)$$

where I is the integrated peak area, S is the corresponding sensitivity factor, and the subscript i and j corresponds to the different elements (e.g., bismuth, sulfur, vanadium). X-ray fluorescence (XRF) measurements were performed by using a Rigaku WD-XRF ZSX Primus II setup. A quantitative analysis was done on the Bi Lα, V Kα, O Kα and S Kα edge with a PC (flow proportional counter, P10 gas detector) and SC (Scintillation counter for heavy elements) detector in a tube above configuration. X-ray diffraction (XRD) measurements were done using a Bruker D8 diffractometer with a Cu Kα radiation (λ = 1.542 Å) at 40 mA and 40 kV. The setup was kept at a grazing incidence configuration (0.5° incident angle). A Horiba HR800 spectrometer (500:1 polarized 20 mW HeNe laser, λ = 632.82 nm) was used for Raman spectroscopy. The morphology of the films were characterized with a LEO GEMINI 1530 scanning electron microscope (SEM) at an acceleration voltage of 5 kV.

Time-resolved microwave conductivity (TRMC) measurements were done in a setup previously described in detail elsewhere.[34, 49] A wavelength tunable optical parametric oscillator (OPO) coupled to a diode pumped Q-switched Nd:YAG laser was used as the excitation source providing 3 ns pulses at 50 Hz repetition rate. A voltage controlled oscillator (SiversIMA VO3262X) generated the microwaves (X-band region, 8.4−8.7 GHz). A microwave cavity cell was used, in which the $BiVO_4$ films deposited on quartz were placed. Carrier transport properties were calculated by taking $BiVO_4$ dielectric constant as 68.[34] Photoelectrochemical (PEC) measurements were conducted in a three-electrode configuration, with the $BiVO_4$ films as the working electrode, a Pt wire as the counter electrode, and an Ag/AgCl electrode (XR300, saturated KCl and AgCl solution, Radiometer Analytical) as the reference electrode. A copper wire and a tin-plated copper foil (CCK-18-101, Farnell) were connected to the exposed FTO to provide electrical contact to the films. The electrolyte was a pH 7 0.1 M

potassium phosphate (KPi) buffer, and 0.5 M sodium sulfite (Na_2SO_3) was added as a hole scavenger. A potentiostat (EG&G PAR 273A) applied the potentials with respect to the reference electrode ($V_{Ag/AgCl}$). This potential was converted to the reversible hydrogen electrode scale (V_{RHE}) by using the Nernst equation:

$$V_{RHE} = V_{Ag/AgCl} + 0.0591 \text{ x pH} + V^0_{Ag/AgCl} \quad (3)$$

where $V^0_{Ag/AgCl}$ is the standard potential of the Ag/AgCl reference electrode (199 mV at 25 °C). Back-side illumination configuration (i.e., light arrives from the substrate-side) was used to measure the photocurrent. The light source is a solar simulator (WACOM, type WXS-50S-5H, class AAA) calibrated to AM1.5 (100 mW cm^{-2}).

BESSY II synchrotron facility (HiKE end station,[50] KMC-1 beamline,[51] Helmholtz-Zentrum Berlin, Germany) was used to carry out the hard-X-ray photoelectron spectroscopy (HAXPES) measurements. At this beamline, photon excitation energies between 2000 and 12000 eV are available. In our measurements, the photon energy used was 4740 eV (first order diffracted light from the Si(311) planes of the double-crystal monochromator). The photoelectrons were detected using a Scienta R4000 optimized for high kinetic energies up to 10000 eV. Binding energy scale calibration was done by measuring the Fermi edge (E_F) of a gold foil. The analysis chamber was kept at ~10^{-8} mbar during all measurements.

Density Functional Theory (DFT) calculation:

Based on the 16 ($BiVO_4$) structural model generated from the $2 \times 1 \times 2$ monoclinic supercell of the pristine $BiVO_4$ monoclinic crystal structure (clinobisvanite phase with space group C2/c) comprising 96 atoms (see Figure 5a), the S-incorporated $BiVO_4$ with the specific stoichiometry of $BiVO_{4-x}S_x$ (x = 0.63) was simulated by substituting 10 O atoms with 10 S atoms at various possible sites inside the pristine supercell. This amount of incorporated sulfur together with the reduced S^{2-} state were chosen based on the obtained XRF and XPS measurements. Representative S-incorporated geometrical configurations revealing more (or less) separated and more (or less) agglomerated S atoms in $BiVO_4$ lattice, namely S-linear, S-random, S-around Bi, S-around V, and well-dispersed S-pairing, were studied. For S-linear model, the 10 S atoms were substituted at O sites located linearly in the same plane. For S-random model, well-separated O sites inside the supercell were randomly substituted by 10 S atoms. For S-around Bi and V models, the 10 S atoms were mostly substituted at O sites surrounding the nearest neighbor Bi and V, respectively. For well-dispersed S-pairing model, the 10 S atoms were homogenously substituted at O sites throughout the lattice, in which each pair of S atoms was located at two O sites bridging 2 Bi.

The geometrical structures were optimized by means of periodic density functional theory (DFT) using VASP program.[52-55] The PBE functional[56] together with the PAW method,[57] 400 eV cutoff energy for basis functions, and 3 x 3 x 3 Monkhorst-Pack k-point mesh[58] for Brillouin zone, were adopted. The configurations for valence electrons treated explicitly in the calculations are $3s^23p^4$ for S, $2s^22p^4$ for O, $3p^63d^44s^1$ for V, and $6s^26p^3$ for Bi. The geometry optimization was considered converged when forces on atoms were near 0.01 eV/Å, the stress was near 0.02 GPa, and the displacement was near 5×10^{-4} Å.

The thermodynamic stability of the most relevant $BiVO_{4-x}S_x$ (x = 0.63) structural configuration was studied using the gas phase molecular sulfur S_2 like doping chemical agent to mimic the experimental protocol adopted for synthesizing this S-incorporated $BiVO_4$ material using this reaction:

$$BiVO_4 + {}^{x}/_{2}\, S_2(g) \rightarrow BiVO_{4-x}S_x + {}^{x}/_{2} O_2(g) \quad (4)$$

The formation energy was computed using this expression:

$$E_{form}(3) = E_{tot}[BiVO_{4-x}S_x] - E_{tot}[BiVO_4] + \tfrac{x}{2}.E_{tot}[O_2] - \tfrac{x}{2}.E_{tot}[S_2] + x.\Delta\mu_O - x.\Delta\mu_S \quad (5)$$

$E_{tot}[BiVO_4]$ and $E_{tot}[BiVO_{4-x}S_x]$ represent the electronic energies of undoped and S-doped materials within the lowest-energy geometries, whereas $E_{tot}[S_2]$ and $E_{tot}[O_2]$ are the total energies of S_2 and O_2 molecules. $\Delta\mu_S$ and $\Delta\mu_O$ are the sulfur and oxygen chemical potentials given by:

$$\Delta\mu_{O,S} = h_{O_2,S_2}(T) - T.s_{O_2,S_2}(T) + R.T.\ln\left[\frac{p(O_2,S_2)}{p_0}\right] \quad (6)$$

The thermal corrections of O_2 and S_2 including the zero-point energy were obtained from DMol program[59] using PBE and DNP basis set.[60] For pristine and S-incorporated materials, the relative difference in the thermal contributions was neglected. The total energies of molecules and solids were obtained from VASP. Here, $\Delta\mu_S$ was fixed at -0.86 eV originated from T = 600 K and $p(S_2) = 3.10^{-4}$ bar to mimic the required experimental conditions. The reference formation energy corresponds to 0 eV for pristine $BiVO_4$. Lower or higher formation energy represents more or less stable material than the pristine $BiVO_4$. This approach has been recently applied to H-doped $BiVO_4$[34] and S-doped TiO_2[61], and could give a rational insight on its thermodynamic behaviors.

The electronic structure features of pristine $BiVO_4$ and $BiVO_{4-x}S_x$ (x = 0.63) materials were investigated through density of states computations using PBE based on the obtained optimized structures. For Brillouin zone integration, the tetrahedron approach along with Blöchl corrections was considered. To guarantee a sufficient convergence of band gap, an increased basis functions cutoff up to 500 eV was taken into consideration. In fact, we are aware that PBE does not give the exact experimental band gap, and this underestimation could be improved using HSE06.[62-67] Here, we aimed at providing a relative trend, and therefore, the HSE06 functional was not applied in our work.

ASSOCIATED CONTENT

In the **Supporting Information** more pictures of $BiVO_4$ films with different sulfur content, as well as further UV-Vis data, XRD, TRMC and PEC and Raman spectra are shown. Furthermore, X-ray absorption spectra and more information on the DFT calculations are provided.

This material is available free of charge via the Internet at http://pubs.acs.org.

AUTHOR INFORMATION

Corresponding Author

E-mail: fatwa.abdi@helmholtz-berlin.de

Author Contributions

The manuscript was written through contributions of all authors. / All authors have given approval to the final version of the manuscript.

Funding Sources

This work was funded by the German Federal Ministry of Education and Research (BMBF), project "MeOx4H2" (03SF0478A) and project "CT-PEC" (01DP14011).

ACKNOWLEDGMENT

We acknowledge Sebastian Schmidt and Sonja Cinque for the assistance with XRF measurements. S.L., L.C. and M.H. thank the KAUST Supercomputing Laboratory for giving the needed computational resources.

REFERENCES

(1) van de Krol, R.; Grätzel M.; Photoelectrochemical Hydrogen Production. *Springer*, New York **2012**.

(2) van de Krol, R.; Parkinson, B. A., Perspectives on the photoelectrochemical storage of solar energy. *MRS Energy Sustain.* **2017,** 4, E13, 1-11.

(3) Sivula, K.; van de Krol, R., Semiconducting materials for photoelectrochemical energy conversion. *Nat. Rev. Mater.* **2016,** *1*, 15010-1-16.

(4) Sivula, K., Metal Oxide Photoelectrodes for Solar Fuel Production, Surface Traps, and Catalysis. *J. Phys. Chem. Lett.* **2013,** 4, 1624-1633.

(5) Zhang, L.; Ye, X.; Boloor, M.; Poletayev, A.; Melosh, N. A.; Chueh, W. C., Significantly enhanced photocurrent for water oxidation in monolithic Mo:$BiVO_4$/SnO_2/Si by thermally increasing the minority carrier diffusion length. *Energy Environ. Sci* **2016,** 9, 2044-2052.

(6) Kudo, A.; Omori, K.; Kato, H., A Novel Aqueous Process for Preparation of Crystal Form-Controlled and Highly Crystalline $BiVO_4$ Powder from Layered Vanadates at Room Temperature and Its Photocatalytic and Photophysical Properties. *J. Amer. Chem. Soc.* **1999,** 121, 11459-11467.

(7) Abdi, F. F.; Han, L.; Smets, A. H. M.; Zeman, M.; Dam, B.; van de Krol, R., Efficient solar water splitting by enhanced charge separation in a bismuth vanadate-silicon tandem photoelectrode. *Nat. Commun.* **2013,** 4, 2195-1-7.

(8) Payne, D. J.; Robinson, M. D. M.; Egdell, R. G.; Walsh, A.; McNulty, J.; Smith, K. E.; Piper, J. F. J., The nature of electron lone pairs in $BiVO_4$, *Appl. Phys. Lett.* **2011**, 98, 212110-1-3.

(9) Pihosh, Y.; Turkevych, I.; Mawatari, K.; Uemura, J.; Kazoe, Y.; Kosar, S.; Makita, K.; Sugaya, T.; Matsui, T.; Fujita, D.; Tosa, M.; Kondo, M.; Kitamori, T., Photocatalytic generation of hydrogen by core-shell WO_3/$BiVO_4$ nanorods with ultimate water splitting efficiency. *Sci. Rep.* **2015,** *5*, 11141-1-10.

(10) van de Krol, R.; Liang, Y.; Schoonman, J., Solar hydrogen production with nanostructured metal oxides. *J. Mater. Chem.* **2008,** 18, 2311-2320.

(11) Shi, X.; Choi, I. Y.; Zhang, K.; Kwon, J.; Kim, D. Y.; Lee, J. K.; Oh, S. H.; Kim, J. K.; Park, J. H., Efficient photoelectrochemical hydrogen production from bismuth vanadate-decorated tungsten trioxide helix nanostructures. *Nat. Commun.* **2014,** 5, 4775-1-8.

(12) Abdi, F. F.; Savenije, T. J.; May, M. M.; Dam, B.; van de Krol, R., The Origin of Slow Carrier Transport in $BiVO_4$ Thin Film Photoanodes: A Time-Resolved Microwave Conductivity Study. *J. Phys. Chem. Lett.* **2013,** 4, 2752-2757.

(13) Kosar, S.; Pihosh, Y.; Bekarevich, R.; Mitsuishi, K.; Mawatari, K.; Kazoe, Y.; Kitamori, T.; Tosa, M.; Tarasov, A. B.; Goodilin, E. A.; Struk, Y. M.; Kondo, M.; Turkevych, I., Highly efficient photocatalytic conversion of solar energy to hydrogen by WO_3/$BiVO_4$ core–shell heterojunction nanorods. *Appl. Nanosci.* **2018,** *8*, 1-8.

(14) Cooper, J. K.; Gul, S.; Toma, F. M.; Chen, L.; Glans, P.-A.; Guo, J.; Ager, J. W.; Yano, J.; Sharp, I. D., Electronic Structure of Monoclinic $BiVO_4$. *Chem. Mater.* **2014,** 26, 5365-5373.

(15) Zhang, M.; Ma, Y.; Friedrich, D.; van de Krol, R.; Wong, L. H.; Abdi, F. F., Elucidation of the opto-electronic and photoelectrochemical properties of $FeVO_4$ photoanodes for solar water oxidation. *J. Mater. Chem. A* **2018,** 6, 548-555.

(16) Loiudice, A.; Ma, J.; Drisdell, W. S.; Mattox, T. M.; Cooper, J. K.; Thao, T.; Giannini, C.; Yano, J.; Wang, L.-W.; Sharp, I. D.; Buonsanti, R., Bandgap Tunability in Sb-Alloyed $BiVO_4$ Quaternary Oxides as Visible Light Absorbers for Solar Fuel Applications. *Adv. Mater.* **2015,** 27, 6733-6740.

(17) Jiao, Z.; Zheng, J.; Feng, C.; Wang, Z.; Wang, X.; Lu, G.; Bi, Y., Fe/W Co-Doped $BiVO_4$ Photoanodes with a Metal–Organic Framework Cocatalyst for Improved Photoelectrochemical Stability and Activity. *ChemSusChem* **2016,** 9, 2824-2831.

(18) Dolgos, M. R.; Paraskos, A. M.; Stoltzfus, M. W.; Yarnell, S. C.; Woodward, P. M., The electronic structures of vanadate salts: Cation substitution as a tool for band gap manipulation. *J. Solid State Chem.* **2009,** 182, 1964-1971.

(19) Xia, C.; Jia, Y.; Tao, M.; Zhang, Q., Tuning the band gap of hematite α-Fe_2O_3 by sulfur doping. *Phys. Lett. A* **2013,** *377*, 1943-1947.

(20) Khan, A.; Ahmed, M. I.; Adam, A.; Azad, A. M.; Qamar, M., A novel fabrication methodology for sulfur-doped ZnO nanorods as an active photoanode for improved water oxidation in visible-light regime. *Nanotechnology* **2017,** 28, 055602.

(21) Rettie, A. J. E.; Klavetter, K. C.; Lin, J.-F.; Dolocan, A.; Celio, H.; Ishiekwene, A.; Bolton, H. L.; Pearson, K. N.; Hahn, N. T.; Mullins, C. B., Improved Visible Light Harvesting of WO_3 by Incorporation of Sulfur or Iodine: A Tale of Two Impurities. *Chem. Mater.* **2014,** 26, 1670-1677.

(22) Zhao, Z.; Dai, H.; Deng, J.; Liu, Y.; Au, C. T., Enhanced visible-light photocatalytic activities of porous olive-shaped sulfur-doped $BiVO_4$-supported cobalt oxides. *Solid State Sci.* **2013,** 18, 98-104.

(23) Guo, M.; Wang, Y.; He, Q.; Wang, W.; Wang, W.; Fu, Z.; Wang, H., Enhanced photocatalytic activity of S-doped $BiVO_4$ photocatalysts. *RSC Adv.* **2015,** 5, 58633-58639.

(24) Gong; H., Freudenberg; N., Nie; M., van de Krol; R., Ellmer; K., $BiVO_4$ photoanodes for water splitting with high injection efficiency, deposited by reactive magnetron co-sputtering. *AIP Adv.* **2016,** 6, 45108-1-10.

(25) Bernechea, M.; Cao, Y.; Konstantatos, G., Size and bandgap tunability in Bi_2S_3 colloidal nanocrystals and its effect in solution processed solar cells. *J. Mater. Chem. A* **2015,** 3, 20642-20648.

(26) Liu, Z.-Q.; Huang, W.-Y.; Zhang, Y.-M.; Tong, Y.-X., Facile hydrothermal synthesis of Bi2S3 spheres and CuS/Bi_2S_3 composites nanostructures with enhanced visible-light photocatalytic performances. *CrystEngComm* **2012,** 14, 8261-8267.

(27) Zhao, Z.; Dai, H.; Deng, J.; Liu, Y.; Au, C.T., Effect of sulfur doping on the photocatalytic performance of $BiVO_4$ under visible light illumination. *Chin. J. Catal.* **2013,** 34, 1617-1626.
(28) Zingg, D. S.; Hercules, D. M., Electron spectroscopy for chemical analysis studies of lead sulfide oxidation. *J.Phys. Chem.* **1978,** 82, , 1992-1995.
(29) Carroll T.X., De J., Maclaren D.C., Thomas T.D., Saethre L. J. Relativistic corrections to reported sulfur 1*s* ionization energies, *J. Electron Spectrosc. Relat. Phemon.* **1987**, 42, 281-284.
(30) J. Berkowitz, J. R. M., Equilibrium Composition of Sulfur Vapor. *J. Chem. Phys.* **1963,** 39, 275-283.
(31) Kröger, F. A., The Chemistry of Imperfect Crystals, *Phys. Today* **1964,** 17, 66-68.
(32) Suryawanshi, M. P.; Ghorpade, U. V.; Shin, S. W.; Gang, M. G.; Wang, X.; Park, H.; Kang, S. H.; Kim, J. H., Enhanced Solar Water Oxidation Performance of TiO_2 via Band Edge Engineering: A Tale of Sulfur Doping and Earth-Abundant CZTS Nanoparticles Sensitization. *ACS Catal.* **2017,** 7, 8077-8089.
(33) Shin, S. W.; Lee, J. Y.; Ahn, K.-S.; Kang, S. H.; Kim, J. H., Visible Light Absorbing TiO_2 Nanotube Arrays by Sulfur Treatment for Photoelectrochemical Water Splitting. *J.Phys. Chem. C* **2015,** 119, 13375-13383.
(34) Jang, J. W.; Friedrich, D.; Müller, S.; Lamers, M.; Hempel, H.; Lardhi, S.; Cao, Z.; Harb, M.; Cavallo, L.; Heller, R.; Eichberger, R.; Krol, R. v. d.; Abdi, F. F., Enhancing Charge Carrier Lifetime in Metal Oxide Photoelectrodes through Mild Hydrogen Treatment *Adv. Energy Mater.* **2017,** 7, 1701536-1-11.
(35) Ge, J.; Roland, P. J.; Koirala, P.; Meng, W.; Young, J. L.; Petersen, R.; Deutsch, T. G.; Teeter, G.; Ellingson, R. J.; Collins, R. W.; Yan, Y., Employing Overlayers To Improve the Performance of Cu_2BaSnS_4 Thin Film based Photoelectrochemical Water Reduction Devices. *Chem. Mat.* **2017,** 29, 916-920.
(36) Su, J.; Wei, Y.; Vayssieres, L., Stability and Performance of Sulfide-, Nitride-, and Phosphide-Based Electrodes for Photocatalytic Solar Water Splitting. *J. Phys. Chem. Lett.* **2017,** 8, 5228-5238.
(37) McDowell, M. T.; Lichterman, M. F.; Spurgeon, J. M.; Hu, S.; Sharp, I. D.; Brunschwig, B. S.; Lewis, N. S., Improved Stability of Polycrystalline Bismuth Vanadate Photoanodes by Use of Dual-Layer Thin TiO_2/Ni Coatings. *J. Phys. Chem. C* **2014,** 118, 19618-19624.
(38) Moehl, T.; Suh, J.; Sévery, L.; Wick-Joliat, R.; Tilley, S. D., Investigation of (Leaky) ALD TiO_2 Protection Layers for Water-Splitting Photoelectrodes. *ACS Appl. Mater. Interfaces* **2017,** 9, 43614-43622.
(39) Kim, T. W.; Choi, K.-S., Improving Stability and Photoelectrochemical Performance of $BiVO_4$ Photoanodes in Basic Media by Adding a $ZnFe_2O_4$ Layer. *J. Amer. Chem. Soc.* **2016,** 7, 447-451.
(40) Bae, D.; Seger, B.; Vesborg, P. C. K.; Hansen, O.; Chorkendorff, I., Strategies for stable water splitting via protected photoelectrodes. *Chem. Soc. Rev.* **2017,** 46, 1933-1954.
(41) Hu, S.; Shaner, M. R.; Beardslee, J. A.; Lichterman, M.; Brunschwig, B. S.; Lewis, N. S., Amorphous TiO_2 coatings stabilize Si, GaAs, and GaP photoanodes for efficient water oxidation. *Science* **2014,** 344, 1005-1009.
(42) Chen, L.; Yang, J.; Klaus, S.; Lee, L. J.; Woods-Robinson, R.; Ma, J.; Lum, Y.; Cooper, J. K.; Toma, F. M.; Wang, L.-W.; Sharp, I. D.; Bell, A. T.; Ager, J. W., p-Type Transparent Conducting Oxide/n-Type Semiconductor Heterojunctions for Efficient and Stable Solar Water Oxidation. *J. Amer. Chem. Soc.* **2015,** 137, 9595-9603.
(43) Yang, J.; Cooper, J. K.; Toma, F. M.; Walczak, Karl A.; Favaro, M.; Beeman, Jeffrey W.; Hess, Lucas H.; Wang, C.; Zhu, C.; Gul, S.; Yano, J.; Kisielowski, C.; Schwartzberg, A.; Sharp, Ian D., A multifunctional biphasic water splitting catalyst tailored for integration with high-performance semiconductor photoanodes. *Nat. Mater.* **2016,** 16, 335-341.
(44) Abdi, F. F.; van de Krol, R., Nature and Light Dependence of Bulk Recombination in Co-Pi-Catalyzed $BiVO_4$ Photoanodes. *J. Phys. Chem. C* **2012,** 116, 9398-9404.
(45) Abdi, F. F.; Nienke, F.; Roel, v. d. K., Efficient $BiVO_4$ Thin Film Photoanodes Modified with Cobalt Phosphate Catalyst and W-doping. *ChemCatChem* **2013,** 5, 490-496.
(46) Wang, F.; Chemseddine, A.; Abdi, F. F.; van de Krol, R.; Berglund, S. P., Spray pyrolysis of $CuBi_2O_4$ photocathodes: improved solution chemistry for highly homogeneous thin films. *J. Mater. Chem. A* **2017,** 5, 12838-12847.
(47) West, W. A.; Menzies, A. W. C., The Vapor Pressures of Sulphur between 100° and 550° with related Thermal Data. *J. Phys. Chem.* **1928,** 33, 1880-1892.
(48) Meyer, B., Elemental sulfur. *Chem. Rev.* **1976,** 76, 367-388.
(49) Kroeze, J. E.; Savenije, T. J.; Warman, J. M., Electrodeless Determination of the Trap Density, Decay Kinetics, and Charge Separation Efficiency of Dye-Sensitized Nanocrystalline TiO2. *J. Amer. Chem. Soc.* **2004,** 126, 7608-7618.
(50) Gorgoi, M.; Svensson, S.; Schäfers, F.; Öhrwall, G.; Mertin, M.; Bressler, P.; Karis, O.; Siegbahn, H.; Sandell, A.; Rensmo, H.; Doherty, W.; Jung, C.; Braun, W.; Eberhardt, W., The high kinetic energy photoelectron spectroscopy facility at BESSY progress and first results. *Nucl. Instrum. Methods Phys. Res.* **2009,** 601, 48-53.
(51) Schaefers, F.; Mertin, M.; Gorgoi, M., KMC-1: A high resolution and high flux soft x-ray beamline at BESSY. *Rev. Sci. Instrum.* **2007,** 78, 123102-1-14.
(52) G. Kresse, J. H., Ab initio molecular-dynamics simulation of the liquid-metal--amorphous-semiconductor transition in germanium. *Phys. Rev. B* **1994,** 49, 14251-14269.
(53) G. Kresse, D. J., From ultrasoft pseudopotentials to the projector augmented-wave method. *Phys. Rev. B* **1999,** 59, 1758-1775.
(54) G. Kresse, J. F., Efficient iterative schemes for ab initio total-energy calculations using a plane-wave basis set. *Phys. Rev. B* **1996,** 54, 11169-11186.
(55) Kresse, G.; Furthmüller, J., Efficiency of ab-initio total energy calculations for metals and semiconductors using a plane-wave basis set. *Comput. Mater. Sci.* **1996,** 6, 15-50.
(56) Perdew, J.P.; Burke, K.; Ernzerhof, M., Generalized Gradient Approximation Made Simple. *Phys. Rev. Lett.* **1996,** 77, 3865-3868.
(57) Blöchl, P. E., Projector augmented-wave method. *Phys. Rev. B* **1994,** 50, 17953-17979.
(58) Monkhorst, H. J.; Pack, J. D. , Special points for Brillouin-zone integrations. *Phys. Rev. B* **1976,** 13, 5188-5192.
(59) Delley, B., From molecules to solids with the DMol3 approach *J. Chem. Phys.* **2000,** 113, 7756-7764.
(60) Delley, B., An all-electron numerical method for solving the local density functional for polyatomic molecules *J. Chem. Phys.* **1990,** 92, 508-517.
(61) Harb, M.; Sautet, P.; Raybaud, P., Anionic or Cationic S-Doping in Bulk Anatase TiO_2: Insights on Optical

Absorption from First Principles Calculations. *J. Phys. Chem. C* **2013,** 117, 8892-8902.
(62) Harb, M.; Masih, D.; Ould-Chikh, S.; Sautet, P.; Basset, J.-M.; Takanabe, K., Determination of the Electronic Structure and UV–Vis Absorption Properties of $(Na_{2-x}Cu_x)Ta_4O_{11}$ from First-Principle Calculations. *J. Phys. Chem. C* **2013,** 117, 17477-17484.
(63) Harb, M.; Masih, D.; Takanabe, K., Screened coulomb hybrid DFT investigation of band gap and optical absorption predictions of $CuVO_3$, $CuNbO_3$ and $Cu_5Ta_{11}O_{30}$ materials. *Phys. Chem. Chem. Phys.* **2014,** 16, 18198-18204.
(64) Lardhi, S.; Curutchet, A.; Cavallo L.; Harb; M.; Le Bahers, T., Ab initio assessment of $Bi_{1-x}RE_xCuOS$ (RE = La, Gd, Y, Lu) solid solutions as a semiconductor for photochemical water splitting *Phys. Chem. Chem. Phys.* **2017**, (19), 12321-12330.
(65) Lardhi, S.; Noureldine, D.; Harb, M.; Ziani, A.; Cavallo, L.; Takanabe, K., Determination of the electronic, dielectric, and optical properties of sillenite $Bi_{12}TiO_20$ and perovskite-like $Bi_4Ti_3O_{12}$ materials from hybrid first-principle calculations *J. Chem. Phys.* **2016,** 144, 134702-1-8.
(66) Noureldine, D.; Lardhi, S.; Ziani, A.; Harb, M.; Cavallo, L.; Takanabe, K., Combined experimental-theoretical study of the optoelectronic properties of non-stoichiometric pyrochlore bismuth titanate. *J. Mater. Chem. C* **2015,** 3, 12032-12039.
(67) Paier, J.; Marsman, M.; Hummer, K.; Kresse, G.; Gerber, I. C.; Ángyán, J. G., Screened hybrid density functionals applied to solids *J. Chem. Phys.* **2006,** 124, 154709-1-13.

Table of Contents graphic